High-resolution simulations of downslope gravity currents in the acceleration phase

Albert Dai

Citation: Physics of Fluids **27**, 076602 (2015); doi: 10.1063/1.4923208
View online: http://dx.doi.org/10.1063/1.4923208
View Table of Contents: http://scitation.aip.org/content/aip/journal/pof2/27/7?ver=pdfcov
Published by the AIP Publishing

PHYSICS OF FLUIDS **27**, 076602 (2015)

High-resolution simulations of downslope gravity currents in the acceleration phase

Albert Dai[a)]
Department of Engineering Science and Ocean Engineering, National Taiwan University, Taipei, Taiwan

(Received 30 January 2015; accepted 4 June 2015; published online 6 July 2015)

Gravity currents generated from an instantaneous buoyancy source propagating down a slope in the range of $0° \le \theta < 90°$ have been investigated in the acceleration phase by means of high-resolution two-dimensional simulations of the incompressible Navier-Stokes equations with the Boussinesq approximation. Front velocity history shows that, after the heavy fluid is released from rest, the flow goes through the acceleration phase, reaching a maximum front velocity $U_{f,max}$, and followed by the deceleration phase. The existence of a maximum of $U_{f,max}$ is found near $\theta = 40°$, which is supported by the improved theory. It is identified for the first time that the time of acceleration decreases as the slope angle increases, when the slope angle is approximately greater than 10°, and the time of acceleration increases as the slope angle increases for gravity currents on lower slope angles. A fundamental difference in flow patterns, which helps explain the distinct characteristics of gravity currents on high and low slope angles using scaling arguments, is revealed. Energy budgets further show that, as the slope angle increases, the ambient fluid is more easily engaged in the gravitational convection and the potential energy loss is more efficiently converted into the kinetic energy associated with ambient fluid. The propagation of gravity currents on a slope is found to be qualitatively modified as the depth ratio, i.e., the lock height to channel height ratio, approaches unity. As the depth ratio increases, the conversion of potential energy loss into the kinetic energy associated with heavy fluid is inhibited and the conversion into the kinetic energy associated with ambient fluid is enhanced by the confinement of the top wall. [http://dx.doi.org/10.1063/1.4923208]

I. INTRODUCTION

Gravity currents, otherwise known as buoyancy or density currents, are flows driven by a density difference mainly in the horizontal direction. The density difference may be attributed to a number of factors, including temperature differentials, dissolved and suspended materials, e.g., salt and sediments. In the literature, gravity currents on a horizontal boundary produced from an instantaneous finite buoyancy source, i.e., lock-exchange flows, have drawn the most attention.[1–9] Gravity currents either down or up a slope are much less considered but are also commonly encountered in geophysical environments and engineering applications.[10–15]

For gravity currents down a slope, the influence of the slope angle on the classical, full-depth, lock-exchange flows has been investigated by Ref. 16 with two-dimensional Navier-Stokes simulations and experiments, where the depth ratio, i.e., the lock height to channel height ratio, was unity and the aspect ratio of released heavy fluid, i.e., the lock length to lock height ratio, was ten. It was found that the flow produced from full lock releases goes through an initial quasi-steady phase with a constant front velocity, which has a maximum for slope angles around 40°, then followed by a transition to a second phase with a larger, unsteady, front velocity. The reason for the transition to a second phase

a)hdai@ntu.edu.tw

is that for such a long lock length, the fluid layers behind the front move faster than the front itself due to streamwise component of the gravity acceleration and eventually the transition is triggered because the front is unable to absorb more fluid from behind. Reference 17 also performed gravity current experiments in tilted tubes. Reference 18 investigated the gravity currents in a cylindrical tube and in a square channel using two-dimensional and three-dimensional simulations. It was reported that two-dimensional simulations correctly predict the acceleration phase and constant front velocity slumping phase, but fail to do so during later stages when the gravity currents decelerate due to the possibility of three-dimensional vortex interactions. Some applications are adequately described by the lock-exchange flows on a slope, such as the propagation of an accidental release of methane in a mine and the spreading of hot combustion products from a tunnel fire.

In other geophysical and geological environments, e.g., in the form of powder snow avalanches, pyroclastic flows, or turbidity currents down the continental slope, the gravity currents down inclined slopes are not confined by the top wall because the height of the flow domain is essentially infinite. Reference 19 investigated the propagation of a fixed, finite volume of heavy fluid down a slope in a channel, where the depth ratios were 0.16 and 0.13 for the two working channels and the aspect ratio of released heavy fluid was 1.25, which is significantly smaller than that in Ref. 16. It is worth noting that in order to model gravity currents in deep ambient, in some experiments such as Refs. 19 and 20, the gravity currents are produced in a tilted channel and the top boundary is parallel to the bottom rather than a horizontal free surface. Even though the ambient depth was essentially finite, the effect of the top boundary was neglected and the influence of the depth ratio was not considered in Ref. 19. One of our objectives in the study, therefore, is to understand how the presence of the top boundary affects the gravity currents when the depth ratio approaches unity. It was reported therein that the thermal theory gives a good description of the gravity currents propagating on a slope, which go through an acceleration phase followed by a deceleration phase. This problem was computationally investigated by Refs. 21 and 22 using two-dimensional and three-dimensional simulations and it has also been confirmed that the three-dimensional interactions are not important as long as the gravity currents remain in the acceleration phase and therefore, two-dimensional simulations are sufficiently representative of the gravity currents in the acceleration phase. This problem was also experimentally revisited by Ref. 23 for larger aspect ratio of released heavy fluid, and it was found that the acceleration distance is increased and the produced gravity currents behave more like a "starting plume," in which a constant buoyancy flux is maintained at the upstream end, as inferred by Ref. 20. The influence of the aspect ratio of released heavy fluid on the lock-exchange flows in deep ambient was also studied by Ref. 24 using two-dimensional Navier-Stokes simulations. More recently, the theoretical work of Refs. 25 and 26 reported that the propagation of gravity currents obeys the thermal theory in the early deceleration phase and deviation from the theory occurs in the late deceleration phase when viscous effects become important. This problem was further extended by Ref. 27 for the influence of density contrast on the propagation of gravity currents on a slope. The influence of density contrast in lock-exchange flows was also demonstrated in Ref. 28.

For the gravity currents propagating on a slope in a semi-infinite domain, Ref. 19 followed the famous Ref. 29 and developed the thermal theory for the gravity currents propagating on a slope in a semi-infinite domain, which has formed the basis for many subsequent studies.[30,31] Figure 1 shows the flow domain in this study and a schematic diagram of the gravity currents in the thermal theory. Please note that the thermal theory was originally developed for the case when the limit $\tilde{h}_0 \ll \tilde{L}_{x_3}$ is approached and the gravity currents were approximated by a semi-elliptical shape with aspect ratio $k = \tilde{H}/\tilde{L}$ during the propagation, where $\tilde{H}$ and $\tilde{L}$ are the height and length of the semi-elliptical head, respectively. In summary, with the Boussinesq approximation, the thermal theory bears on the principles of momentum conservation, i.e.,

$$\frac{d\tilde{\rho}_0(1+k_v)S_1\tilde{H}\tilde{L}\tilde{U}}{d\tilde{t}} = \tilde{B}\sin\theta, \tag{1}$$

and mass conservation, i.e.,

$$\frac{d}{d\tilde{t}}(S_1\tilde{H}\tilde{L}) = S_2(\tilde{H}\tilde{L})^{1/2}\alpha(\theta)\tilde{U}. \tag{2}$$

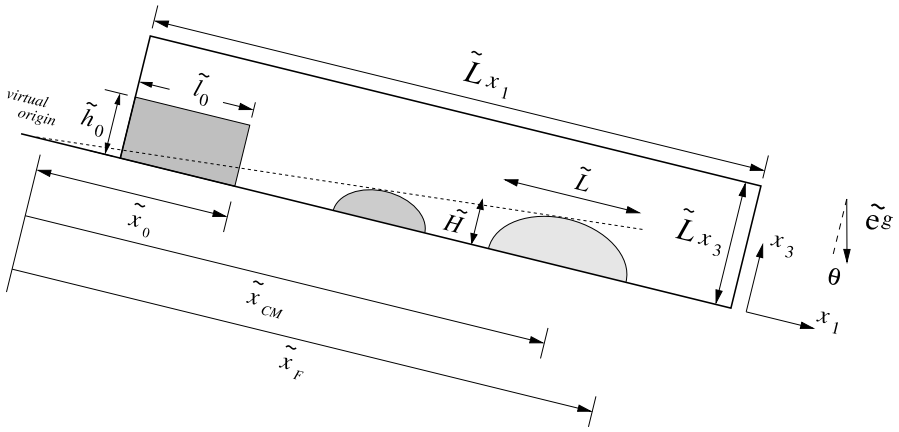

FIG. 1. Sketch for the gravity current propagating on a sloping boundary. Streamwise and wall-normal directions are denoted by x_1 and x_3, respectively. The domain of interest is set as $\tilde{L}_{x_1} \times \tilde{L}_{x_3}$, where $\tilde{L}_{x_1} = 10\tilde{l}_0$, $\tilde{L}_{x_3} = \tilde{h}_0\phi^{-1}$, and ϕ is the lock height to channel height ratio. Heavy fluid initially occupies the shaded region of $\tilde{h}_0 \times \tilde{l}_0$ without momentum. At $t = 0$, the heavy fluid is instantaneously released and begins to propagate in the downslope direction, x_1. The gravity current head approximately takes the form of a semi-elliptical shape, with height $\tilde{H}$ and length $\tilde{L}$. The channel is inclined so the gravity vector $\tilde{e}^g$ makes an angle θ with the wall-normal direction, x_3.

Here, the density of ambient fluid is taken as $\tilde{\rho}_0$ and the density of heavy fluid in the lock region is $\tilde{\rho}_1$, where $(\tilde{\rho}_1 - \tilde{\rho}_0) \ll \tilde{\rho}_0$. The total buoyancy is defined to be $\tilde{B} = (\tilde{\rho} - \tilde{\rho}_0)S_1\tilde{H}\tilde{L}$. The cross-sectional area and the circumference of the semi-elliptical head are defined as $S_1\tilde{H}\tilde{L}$ and $S_2(\tilde{H}\tilde{L})^{1/2}$, respectively, where $S_1 = \pi/4$ and $S_2 = (\pi/2^{3/2})(4k^2 + 1)^{1/2}/k^{1/2}$ are the shape factors. In addition, $\tilde{U}$ is the velocity of the centre of mass of the head, $k_v = 2k$ is the added mass coefficient,[32] and α is the entrainment coefficient.[33] Equation (2) yields self-similar solutions for $\tilde{H}$ and $\tilde{L}$ that grow linearly with distance, and the "virtual origin," is a fictitious location where $\tilde{H} = 0$ by extrapolating $\tilde{H}$ in the upstream direction.

Finally, when the current starts from rest, the centre of mass velocity normalized by the velocity scale, $\sqrt{\tilde{g}_0'\tilde{h}_0}$, is

$$U = \left[C\left(\frac{1}{X_B} - \frac{1}{X_B^4}\right)\right]^{1/2}, \quad C = \frac{(8S_1\tilde{B}\sin\theta)}{(3\tilde{\rho}_0(1 + k_v)\alpha^2 S_2^2\tilde{x}_0\tilde{g}_0'\tilde{h}_0)}, \tag{3}$$

where C is a function of θ, $\tilde{x}_0$ is the distance from the virtual origin to the gate of release, and $X_B = \tilde{x}_{CM}/\tilde{x}_0$. The front location, when measured from the virtual origin, is related to the position of the centre of mass by $\tilde{x}_F = (1 + \alpha S_2/4k^{1/2}S_1)\tilde{x}_{CM}$. Therefore, the front velocity U_f, sometimes referred to as the Froude number, is related to the centre of mass velocity by $U_f = (1 + \alpha S_2/4k^{1/2}S_1)U$.

In fact, the solution to the thermal theory, i.e., (3), predicts that gravity currents on a slope initially go through an acceleration phase followed by a deceleration phase. Of particular interest here is the maximum front velocity,

$$U_{f,max} \approx 0.69(1 + \frac{1}{4}\frac{\alpha S_2}{k^{1/2}S_1})\sqrt{C}, \tag{4}$$

which is novelly derived here by evaluating (3) at the position where velocity gradient vanishes. It is worth noting that the maximum front velocity is, in general, neither a constant nor a monotonically increasing function of $\sqrt{\sin\theta}$, since the right hand side of (4) involves variables that are functions of the slope angle. Reference 19 found the relationship between the front velocity and the front position in the deceleration phase but the existence of a maximum $U_{f,max}$ was not specified unequivocally possibly due to substantial scatter in the experimental data.

Other studies that are related to the present work include, Refs. 34 and 35 who found similarity solutions of the shallow-water equations. Reference 36 investigated the gravity currents produced

from an instantaneous release of buoyancy propagating on a vertically and laterally unconfined uniform slope and developed a theoretical model in the same spirit of thermal theory by Ref. 19.

The present study is a computational extension of the studies reported by Ref. 19 and by Ref. 26. The primary objective is to investigate the influence of the slope angle in the entire range of $0° \le \theta < 90°$, the depth ratio $\phi = \tilde{h}_0/\tilde{L}_{x_3}$, and the Reynolds number Re on the initial development of gravity currents. The lock length here follows Refs. 19 and 26 and remains $l_0 = \tilde{l}_0/\tilde{h}_0 = 1.25$ in this study. In what follows, we outline the numerical formulation of the problem in Sec. II and the results and analysis are presented in Sec. III. Since the focus is on the acceleration phase of the downslope gravity currents and it has been shown that two-dimensional simulations are sufficiently representative in this flow regime, the investigation is conducted by means of high-resolution two-dimensional Navier-Stokes simulations.

II. NUMERICAL FORMULATION

Figure 1 gives a sketch of the configuration for simulations of gravity currents down slopes. The heavy fluid of density $\tilde{\rho}_1$ is confined in the lock region and separated from the light fluid of density $\tilde{\rho}_0$. Here we adopt the Boussinesq approximation, in that the density difference is assumed sufficiently small such that the influence of density variations is retained only in the buoyancy term but neglected in the inertia and diffusion terms. Consequently, the governing equations take the form

$$\frac{\partial u_k}{\partial x_k} = 0, \tag{5}$$

$$\frac{\partial u_i}{\partial t} + \frac{\partial (u_i u_k)}{\partial x_k} = \rho e_i^g - \frac{\partial p}{\partial x_i} + \frac{1}{Re}\frac{\partial^2 u_i}{\partial x_k \partial x_k}, \tag{6}$$

$$\frac{\partial \rho}{\partial t} + \frac{\partial (\rho u_k)}{\partial x_k} = \frac{1}{Pe}\frac{\partial^2 \rho}{\partial x_k \partial x_k}. \tag{7}$$

Here u_i denotes the velocity, ρ the density, e_i^g the unit vector in the direction of gravity, and p the pressure. The set of equations (5)-(7) is made dimensionless by the lock height, $\tilde{h}_0$, as the length scale and the buoyancy velocity,

$$\tilde{u}_b = \sqrt{\tilde{g}_0' \tilde{h}_0}$$

with (8)

$$\tilde{g}_0' = \tilde{g}\frac{\tilde{\rho}_1 - \tilde{\rho}_0}{\tilde{\rho}_0},$$

as the velocity scale. The dimensionless density, i.e., the concentration of fluid mixture, is given by

$$\rho = \frac{\tilde{\rho} - \tilde{\rho}_0}{\tilde{\rho}_1 - \tilde{\rho}_0}. \tag{9}$$

The Reynolds number Re and the Péclet number Pe arising in the dimensionless equations are defined by

$$Re = \frac{\tilde{u}_b \tilde{h}_0}{\tilde{\nu}}$$

and (10)

$$Pe = \frac{\tilde{u}_b \tilde{h}_0}{\tilde{\kappa}},$$

respectively. The two fluids are assumed to have identical kinematic viscosities $\tilde{\nu}$ and diffusion coefficients $\tilde{\kappa}$. They are related by the Schmidt number

$$Sc = \frac{\tilde{\nu}}{\tilde{\kappa}}, \tag{11}$$

which represents the ratio of the kinematic viscosity to molecular diffusivity. Typically in saline experiments, $Sc \approx 700$, but it has been observed by many researchers[37–40] that the influence of Schmidt

number on the dynamics of the gravity current is weak as long as $Sc \approx O(1)$ or larger. Therefore, we follow suit here and employ $Sc = 1$ in the simulations.

The set of equations in the velocity-pressure formulation is solved in the flow domain with resolution $N_{x_1} \times N_{x_3}$. The channel running length in the streamwise direction, L_{x_1}, was chosen ten times larger than the length of the lock to allow full development of the acceleration phase. The depth ratio is ϕ, i.e., $\phi = \tilde{h}_0/\tilde{L}_{x_3}$, in other words the dimensionless height of the channel is $L_{x_3} = \phi^{-1}$, where $\phi \leq 1$. Fourier expansion with the periodic boundary condition is employed in the streamwise direction.[41] To ensure a reflection condition at the left wall ($x_1 = 0$) as in the experiments and to prevent any upslope propagation upon the release of heavy fluid, an image is placed to the left of the domain of interest such that the heavy fluid in the lock is fully discharged into the channel of length L_{x_1}.[22] Chebyshev expansion with Gauss-Lobatto quadrature points is employed in the wall-normal direction. The Gauss-Lobatto quadrature points provide a straightforward implementation of boundary conditions and have high resolution near the walls. Here we employ no-slip and no-flux conditions at the top and bottom walls for the velocity and density fields, respectively. The influence of boundary conditions will not be discussed here, since previous computational investigations, including Refs. 21 and 41, have done so and have shown that the dominant qualitative features of the flow are unchanged, except that gravity currents with slip conditions propagate faster than those with no-slip conditions.

The flow field is advanced in time by the low-storage third-order Runge-Kutta scheme.[42] The convection and buoyancy terms are treated explicitly while the diffusion terms are treated implicitly with Crank-Nicolson scheme. To reduce the aliasing error, Arakawa method[43] is used to evaluate the convection term alternately between divergence and convective forms. The de-aliased pseudospectral code has been employed in Refs. 39 and 44 for lock-exchange flows and in Refs. 21 and 22 for gravity currents down sloping boundaries. In all simulations, the velocity field was initialized with quiescent conditions everywhere. The initial density field is prescribed unity in the heavy fluid region and zero elsewhere with a smooth error-function type transition in the interface region.[45] With increasing Re, the complexity and required resolution increase. To resolve the flow structures of the gravity currents in the domain $L_{x_1} \times L_{x_3} = 10 l_0 \times \phi^{-1}$, adequate resolution requires a grid size of $\Delta x_1 \approx (Re\, Sc)^{-1/2}$ in the streamwise direction[37,41] and the grids $N_{x_1} \times N_{x_3}$ used in Sec. III are listed in Table I. The time step was chosen to produce a Courant number less than 0.5.

III. RESULTS

A. Overview

We begin by describing results from a representative case of the gravity current propagating on a 9° slope with $\phi = 0.16$, as considered experimentally by Refs. 19 and 26. As we will discuss the influence of the depth ratio later in Sec. III E, when the depth ratio is $\phi = 0.16$, the gravity currents fill

TABLE I. Table showing parameters used in the two-dimensional simulations referred to in different sections, including the Reynolds number Re, depth ratio ϕ, slope angle θ, and computational grid $N_{x_1} \times N_{x_3}$. The computational domain is $L_{x_1} \times L_{x_3} = 10 l_0 \times \phi^{-1}$ and the lock length is maintained fixed as $l_0 = 1.25$ for all simulations.

Sections	Re	ϕ	θ (deg)	$N_{x_1} \times N_{x_3}$
III A–III D	4 000	0.16	0-90	672 × 768
III E	4 000	0.075	9	672 × 1232
III E	4 000	0.4	9	672 × 320
III E	4 000	0.7	9	672 × 192
III E	4 000	1.0	9	672 × 128
III F	100	0.16	9	132 × 132
III F	1 000	0.16	9	384 × 384
III F	10 000	0.16	9	1232 × 1232

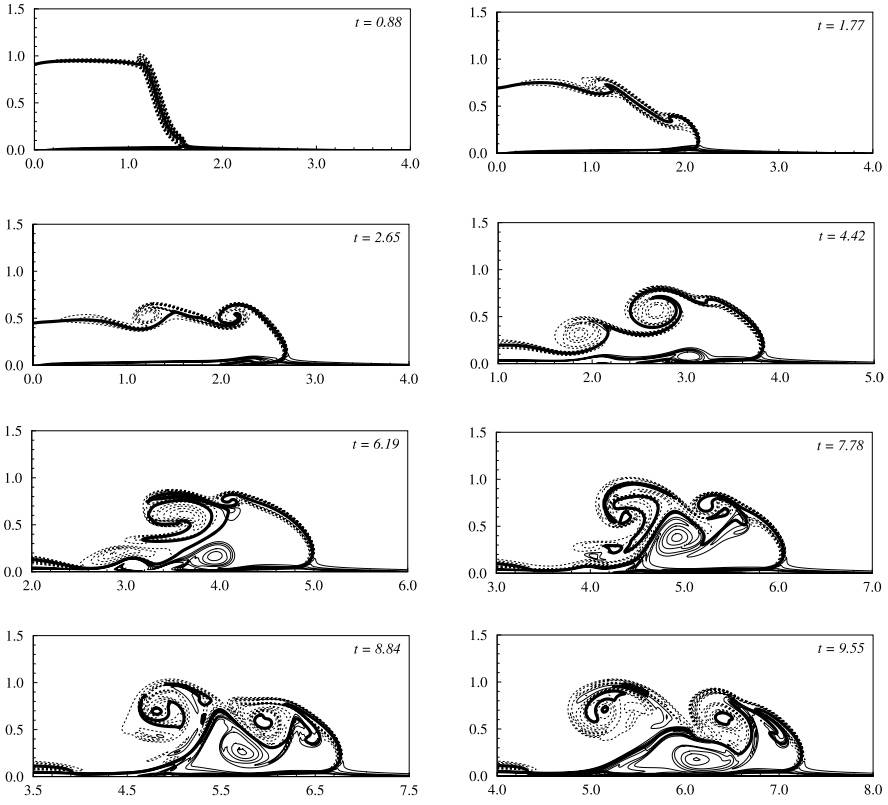

FIG. 2. A gravity current propagating on a 9° slope at $Re = 4000$. Flow evolution is visualized by the density and vorticity contours. Here the thick solid lines represent $\rho = 0.5$ and thin solid (dashed) lines represent positive (negative) vorticity contours. Time instances are chosen at $t = 0.88, 1.77, 2.65, 4.42, 6.19, 7.78, 8.84$, and 9.55.

less than a quarter of the whole depth of the channel and the influence of the top boundary can be neglected.[19,20,46] In the following presentation of the results, unless otherwise specified, we will use only dimensionless variables, where the velocity scale is $\tilde{u}_b$, the length scale is $\tilde{h}_0$, the time scale is $\tilde{h}_0/\tilde{u}_b$, and others as specified in Sec. II. Figure 2 shows the density and vorticity contours for $Re = 4000$. It is observed that, following the release of buoyancy, the heavy fluid collapses and forms a bell shape, as shown in Figure 2 at $t = 0.88$. At this stage, the current head has not yet been fully developed. As time progresses, the heavy fluid continues to slump and push out the head. Spanwise vorticity is generated along the interface between the heavy and ambient fluids and the interface begins to roll up, as shown in Figure 2 at $t = 1.77$. It is observed here that the two roll-up vortices accomplish a complete overturn in the leapfrog process and a large roller is left behind the current front, as shown in Figure 2 at $t = 2.65$–9.55. Recent experiments consistently showed that a large roller takes form at the end of the acceleration phase for the gravity current on a 9° slope, as illustrated in Figure 3 for the reader's convenience, cf. Figure 2 in Ref. 26. In the laboratory, the maximum slope angle was

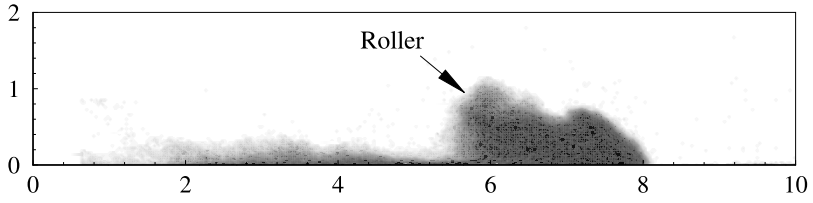

FIG. 3. Image from the experiment 10/03/12-1 reported by Ref. 26 for the gravity current from a buoyancy source of $\tilde{l}_0/\tilde{h}_0 = 10$ cm/8 cm and $\tilde{g}_0' = 17.11$ cm s^{-2} propagating on a 9° slope. Distances in the downslope and wall-normal directions are normalized by the lock height, $\tilde{h}_0$. Time instance is chosen at $t \approx 9.5$ dimensionless units. Reynolds number in the experiment is at $Re \approx 9400$.

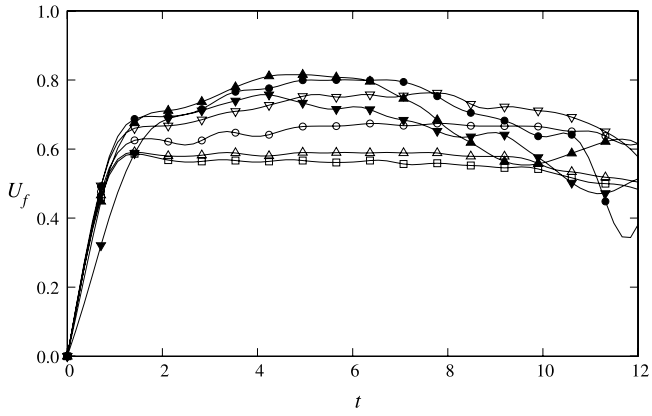

FIG. 4. Dimensionless front velocity versus time for gravity currents propagating on a number of different slope angles with $\phi = 0.16$ and $Re = 4000$. Symbols: □, $\theta = 0°$; △, $\theta = 2°$; ○, $\theta = 9°$; ▽, $\theta = 20°$; ●, $\theta = 30°$; ▲, $\theta = 50°$; ▼, $\theta = 70°$.

limited by the flume height, whereas here we may investigate the gravity currents in the entire range of slope angles with simulations.

In order to unambiguously measure the front location of gravity currents, we follow the robust procedure using the equivalent height,[1,16,22,39] which is defined as

$$h(x_1,t) = \int_0^{L_{x_3}} \rho(x_1,x_3,t)dx_3. \tag{12}$$

The front velocity, U_f, can then be derived using the front location data, via $U_f = dx_f/dt$. Figure 4 shows the front velocity versus time for gravity currents on a number of slope angles. After the heavy fluid is released, the front velocity rapidly increases from zero with maximum acceleration until $t \approx 1.4$. In this initial part of acceleration phase with maximum acceleration, the velocity history is not very sensitively influenced by the variation of the slope angle. In the latter part of the acceleration phase, $t \gtrsim 1.4$, the acceleration is reduced and a maximum front velocity, $U_{f,max}$, is reached. For example, when $\theta = 50°$, the gravity current reaches a maximum front velocity $U_{f,max} \approx 0.81$ at $t \approx 5.13$. It is found here that the aforementioned leapfrog process of roll-up vortices takes place in the latter part of the acceleration phase and the formation of a "cloud" shape in the gravitational convection is persistently observed at the end of the acceleration phase for all slope angles approximately greater than 6°, as illustrated in Figure 5. In the deceleration phase, the two-dimensional simulations present strong time variation in the front velocity, e.g., the abrupt decrease in the front velocity at $t \approx 11$ for $\theta = 30°$ in Figure 3, due to long-lasting vortex interaction, which is mitigated or absent in the three-dimensional simulations because stretching and breakdown of vortices are at work in the deceleration phase.[22,39] For the cases when $\theta = 0°, 2°$, the gravity currents do not continue to accelerate following the initial part of the acceleration phase but move into the slumping phase at a nearly constant speed, as reported previously for partial-depth lock-exchange flows by Ref. 2.

B. Influence of the slope angle

The influence of the slope angle on the maximum front velocity, $U_{f,max}$, is shown in Figure 6(a) with $\phi = 0.16$ and $Re = 4000$. Our simulation results are in qualitatively good agreement with previous experimental data.[19,26] However, it should be pointed out that there exists a discrepancy between the available experimental data and the simulation results and presently the cause of the discrepancy still cannot be identified. The maximum front velocity, which is associated with finite-differencing the data, shows larger scatter than the time of acceleration on large slopes. Increase in the Reynolds number in the simulations results in insignificant increase in the maximum front velocity, which will be discussed later in Sec. III F. Due to the substantial scatter in the experimental data and the limited range of slope angle, previously the existence of a maximum of $U_{f,max}$ in Ref. 19 and in Ref. 26 was

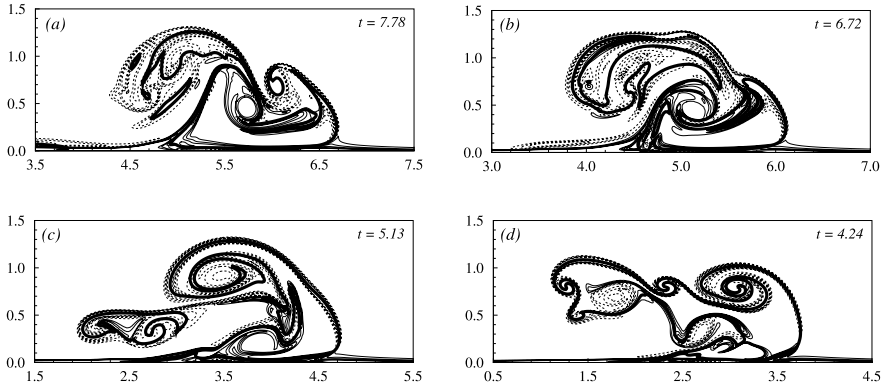

FIG. 5. Flow patterns on different slope angles, i.e., $\theta = 20°$ (a), 30° (b), 50° (c), 70° (d), with $\phi = 0.16$ and $Re = 4000$ visualized at the times when the maximum front velocity $U_{f,max}$ is reached. Flow patterns are visualized by the density and vorticity contours. Here, the thick solid lines represent $\rho = 0.5$ and thin solid (dashed) lines represent positive (negative) vorticity contours. Time instances are chosen at $t = 7.78, 6.72, 5.13,$ and 4.24 for $\theta = 20°$ (a), 30° (b), 50° (c), and 70° (d), respectively.

not concluded unequivocally. It is observed here from the simulation results that a maximum of $U_{f,max}$ exists near $\theta = 40°$, with little variation between 35° and 50°.

To further support the findings of a maximum of $U_{f,max}$ on a theoretical basis, we make use of the formula for $U_{f,max}$, (4), while incorporating the entrainment coefficient and aspect ratio of the head that are functions of the slope angle. With the reported experimental data, cf. Table 1 in Ref. 19, the entrainment coefficient and the aspect ratio of the head incorporated into (4) as $\alpha = 0.3380(\theta\pi/180) + 0.0408$ and $k = -0.1313(\theta\pi/180)^2 + 0.4011(\theta\pi/180) + 0.2061$, respectively, which are best fit for the experimental measurements and the slope angle are in units of degree. Fortuitously, the novelly derived formula for $U_{f,max}$ shows that a maximum front velocity exists around $\theta \approx 49°$, with little variation between 40° and 60°, as shown by the solid line in Figure 6(a). In comparison, the full-depth lock-exchange flows in sloping channels reported by Ref. 16 go through an initial quasi-steady phase with a constant front velocity, and this quasi-steady front velocity also has a maximum for slope angles around $\theta = 40°$. The findings on the influence of the slope angle in Ref. 16 are similar, which is perhaps surprising, considering that the depth ratio $\phi = 1$ and the aspect ratio of released heavy fluid $l_0 = 10$ in Ref. 16 make their configuration quite different from the present set-up.

Figure 6(b) shows the dependence of the time of acceleration, t_c, i.e., when the maximum front velocity is reached, on the slope angle with $\phi = 0.16$ and $Re = 4000$. Our computational data show a surprisingly consistent relationship between the time of acceleration and the slope angle as the

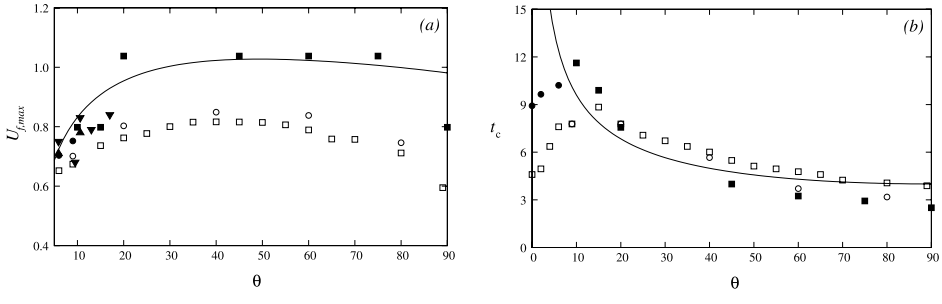

FIG. 6. Maximum dimensionless front velocity $U_{f,max}$ (a) and dimensionless time of acceleration t_c (b) as functions of the slope angle, in units of degree, with $l_0 = 1.25$, $\phi = 0.16$, and $Re = 4000$. A maximum of $U_{f,max}$ exists near $\theta = 40°$ and a maximum of t_c exists near $\theta = 10°$. Symbols: □, computational data at $Re = 4000$; ○, computational data at $Re = 10^4$; ■, experimental data from Ref. 19 for $l_0 = 1.25$ at $Re \approx 10^4$; ●, experimental data from Ref. 26 for $l_0 = 1.25$ at $Re \approx 9400$; ▼, experimental data from Refs. 23 and 47 for $l_0 \approx 2$ at $Re \approx 10^4$; ▲, experimental data from Ref. 47 for $l_0 \approx 1$ at $Re \approx 10^4$. Solid lines in (a) and (b) represent theory (4) and scaling law (13), respectively.

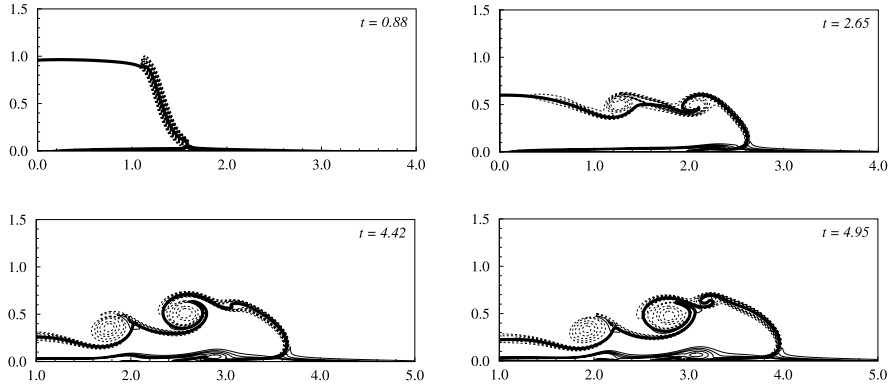

FIG. 7. A gravity current propagating on a 2° slope at $Re = 4000$. Flow evolution is visualized by the density and vorticity contours. Here, the thick solid lines represent $\rho = 0.5$ and thin solid (dashed) lines represent positive (negative) vorticity contours. Time instances are chosen at $t = 0.88, 2.65, 4.42$, and 4.95.

experimental data. It is worth noting that for slope angles approximately greater than 10°, the time of acceleration decreases as the slope angle increases. However, for lower slope angles, the time of acceleration increases as the slope angle increases. A simple scaling argument allows us to estimate the relationship between the time of acceleration and the slope angle. In line with the thermal theory, the gravity currents are driven by the streamwise component of gravity, i.e., $\tilde{g}_0' \sin\theta$. With the length scale taken as $\tilde{h}_0$, an acceleration time can be estimated as

$$\tilde{t}_c \sim \frac{1}{\sqrt{\sin\theta}} \sqrt{\frac{\tilde{h}_0}{\tilde{g}_0'}}, \tag{13}$$

which indicates that the dimensionless time of acceleration t_c scales as $1/\sqrt{\sin\theta}$ and is in good agreement with the experimental and computational data for slope angles greater than approximately 10°, as shown by the solid line in Figure 6(b).

Interestingly, the question concerning the time of acceleration for gravity currents on low slope angles naturally arises. The departure of the time of acceleration from scaling law (13) for low slope angles surely deserves an explanation. To shed some light on the underlying mechanism of initiation of the gravity currents on low slope angles, Figure 7 shows the density and vorticity contours with $\theta = 2°$, $\phi = 0.16$, and $Re = 4000$. In Figure 7, the interface roll-up process is similar to that shown in Figure 2 until $t \approx 4.42$, but here the roll-up vortices do not accomplish a complete overturn and both vortices are left behind the head, as shown in Figure 7 at $t = 4.95$ when the maximum front velocity is reached. Experiments consistently showed that at low slope angles, the gravity current head maintains a more streamlined shape without a large roller, cf. Figure 10 in Ref. 26. The observation made available by the simulations explains the fundamental difference in flow patterns between gravity currents on high and low slope angles. For gravity currents on high slope angles, the heavy fluid convects in the form of a "cloud" shape, which, as assumed, is driven by the streamwise component of gravity, i.e., $\tilde{g}_0' \sin\theta$. For gravity currents on low slope angles, the heavy fluid tends to spread on the slope as in the lock-exchange problem and the flow is mainly driven by the wall-normal component of gravity, i.e., $\tilde{g}_0' \cos\theta$, and as such the time of acceleration increases with increasing slope angle. Therefore, based on the distinct flow patterns and the scaling arguments, the relationship between the time of acceleration and the slope angle is apparently different in the two situations.

C. Mixing

As modeled by the theory, it is known that entrainment of ambient fluid is a major retarding mechanism in the propagation of gravity currents on a slope. As shown in Figures 2 and 7, large-scale vortex overturn events contribute to the mixing of fluids in the acceleration phase and are influenced by the slope angle. It is worth noting that such large-scale vortex structures are predominantly

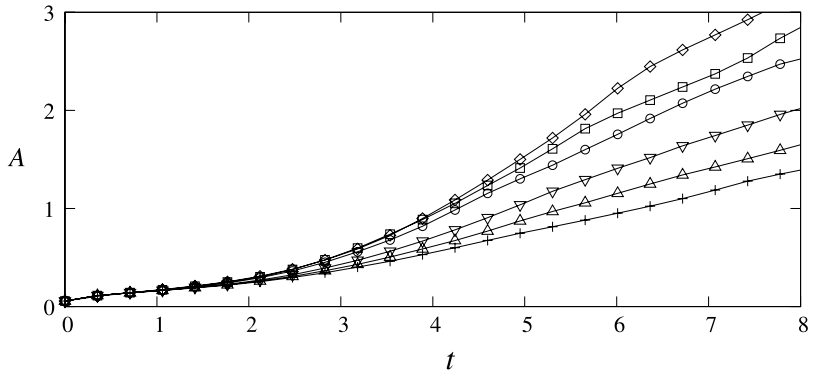

FIG. 8. The dimensionless size of the mixed region versus time for gravity currents on slopes with $\phi = 0.16$ and $Re = 4000$. Six different slope angles are chosen for illustrative purposes. Symbols: +, $\theta = 2°$; △, $\theta = 10°$; ▽, $\theta = 20°$; ○, $\theta = 40°$; □, $\theta = 60°$; ◇, $\theta = 80°$.

two-dimensional in the acceleration phase but are subject to three-dimensional vortex breakdown in the deceleration phase in three-dimensional simulations.[22,39] In order to quantify this observation, we define the mixed region of which the density is within the range of

$$\tilde{\rho}_0 + \frac{1}{10}\Delta\tilde{\rho} < \tilde{\rho} < \tilde{\rho}_1 - \frac{1}{10}\Delta\tilde{\rho}, \tag{14}$$

where $\Delta\tilde{\rho} = \tilde{\rho}_1 - \tilde{\rho}_0$. Please note that (14) is in essence equivalent to $0.1 < \rho < 0.9$ but the cut-off values, that are chosen for illustrative purposes following Ref. 16, do not change the qualitative features of the relationship between the size of the mixed region and time. Figure 8 shows the size of mixed region versus time on different slope angles, where the size of mixed region is made dimensionless by the square of the length scale, i.e., $\tilde{h}_0^2$. It is observed that in the initial part of the acceleration phase, i.e., $0 \le t \lesssim 1.4$, the size of mixed region is not sensitively influenced by the slope angle, while in the latter part of the acceleration phase, the size of mixed region increases uniformly with increasing slope angle. Our results are consistent with previous experimental and computational observations that the vortex interactions and mixing are enhanced at larger slope angles.[16,33,48]

D. Energy budgets

From the point of view of energy budgets, the propagation of gravity currents on an inclined boundary is essentially a conversion process of the available potential energy into kinetic energy and subsequently into dissipation by viscous friction. However, information on the energy budgets can be very difficult to attain in the experiments. In the following, we will provide a computational analysis of the overall energy budget.

The equation for the time derivative of the kinetic energy is obtained by multiplying momentum equation (6) by u_i, i.e.,

$$\frac{D}{Dt}\left(\frac{1}{2}u_i u_i\right) = -\frac{\partial}{\partial x_i}(pu_i) + \frac{2}{Re}\frac{\partial}{\partial x_j}(s_{ij}u_i) - \frac{2}{Re}s_{ij}s_{ij} + \rho(\sin\theta u - \cos\theta w), \tag{15}$$

where D/Dt denotes the material derivative and s_{ij} denotes the strain rate tensor, $s_{ij} = \frac{1}{2}(u_{i,j} + u_{j,i})$. Integration of (15) over the entire flow domain Ω leads to the evolution equation of the total kinetic energy K, i.e.,

$$\frac{dK}{dt} = -\frac{2}{Re}\int_\Omega s_{ij}s_{ij}dV + \int_\Omega \rho(\sin\theta u - \cos\theta w)\,dV, \quad K(t) = \int_\Omega \frac{1}{2}u_i u_i dV, \tag{16}$$

where the divergence terms on the right-hand side of (15) vanish after integration. By weighting the kinetic energy with the dimensionless density, we can associate a fraction of the kinetic energy with

heavy fluid, i.e.,

$$K_H = \int_\Omega \frac{1}{2}\rho u_i u_i dV, \tag{17}$$

and the remainder of the total kinetic energy is associated with ambient fluid, i.e., $K_L = K - K_H$. When the effects of diffusion in the density field on the potential energy are neglected,[41,49] the time derivative of the potential energy in the system is

$$\frac{dE_p}{dt} = -\int_\Omega \rho\,(\sin\,\theta u - \cos\,\theta w)\,dV, \quad E_p(t) = \int_\Omega \rho[x_3\cos\,\theta + (L_{x_1} - x_1)\sin\,\theta]dV. \tag{18}$$

The first term on the right-hand side of (16) represents the dissipation and we use E_d to denote the time integral of dissipation, i.e.,

$$E_d(t) = \int_0^t \epsilon(\tau)d\tau, \quad \epsilon = \frac{2}{Re}\int_\Omega s_{ij}s_{ij}dV. \tag{19}$$

By weighting the time integral of dissipation with the dimensionless density, we can associate a fraction of the time integral of dissipation with heavy fluid, i.e.,

$$E_{dH} = \int_0^t \epsilon_H(\tau)d\tau, \quad \epsilon_H = \frac{2}{Re}\int_\Omega \rho s_{ij}s_{ij}dV, \tag{20}$$

and the remainder of the dissipated energy is associated with ambient fluid, i.e., $E_{dL} = E_d - E_{dH}$. In other words, Equation (16) is essentially a statement of conservation of energy, i.e., that $K + E_p + E_d$ is a constant during the propagation of gravity currents.

Figure 9 shows the time histories of the normalized kinetic energy and dissipated energy during the propagation of gravity currents with $\phi = 0.16$ and $Re = 4000$ on three different slope angles, i.e., $\theta = 9°, 40°$, and $60°$. The acceleration times for $\theta = 9°, 40°$, and $60°$ are $t_c = 7.78, 6.01$, and 4.77, respectively. For convenient comparison among the three cases, the energy budgets are plotted for and normalized with the potential energy drop during the initial eight dimensionless time units. Here, the superscript n denotes normalized contributions. The overall energy is conserved with high accuracy in the acceleration phase and the maximum error is within 1%. It is observed that, as the slope angle increases, less fraction of potential energy loss is converted into the kinetic energy associated with heavy fluid, i.e., K_H^n, and more fraction of potential energy loss is converted into the kinetic energy associated with ambient fluid, i.e., K_L^n, as the gravity currents propagate downslope in the acceleration phase. For slope angles less than 40°, K_H^n grows faster than K_L^n initially before K_L^n overtakes K_H^n towards the end of the acceleration phase. When the slope angle is approximately near 40°, the kinetic energy is equally distributed between the heavy fluid and the ambient fluid after the release of heavy fluid, before K_L^n exceeds K_H^n towards the end of the acceleration phase. As the slope angle increases beyond 40°, the kinetic energy associated with heavy fluid is persistently lower than that associated with ambient fluid. The normalized dissipated energy, E_d^n, decreases as the slope angle increases, while the heavy fluid dissipates more energy than the ambient fluid in the acceleration phase. In summary, in the gravity current propagation the potential energy loss is converted into the kinetic energies associated with heavy and ambient fluids simultaneously before ultimately dissipated. However, as the slope angle increases, the ambient fluid is more easily engaged via interface roll-up and vortex overturns, as the size of mixed region shows in Sec. III C, and the potential energy loss is more efficiently converted into the kinetic energy associated with ambient fluid. The energy analysis indicates that, for sufficiently large slope angles, the ambient fluid could gain more kinetic energy from the available potential energy than the heavy fluid right from the outset, which also supports the findings of the existence of a maximum of $U_{f,max}$ near $\theta = 40°$.

E. Influence of the depth ratio ϕ

As mentioned in the Introduction, depending on the environment, gravity currents on an inclined boundary can be vertically confined ($\phi \approx 1$) in a tunnel, or unconfined ($\phi \ll 1$) in deep ambient. In the following, we will discuss the influence of depth ratio by analyzing the front velocity histories and energy budgets of the gravity currents propagating on a 9° slope.

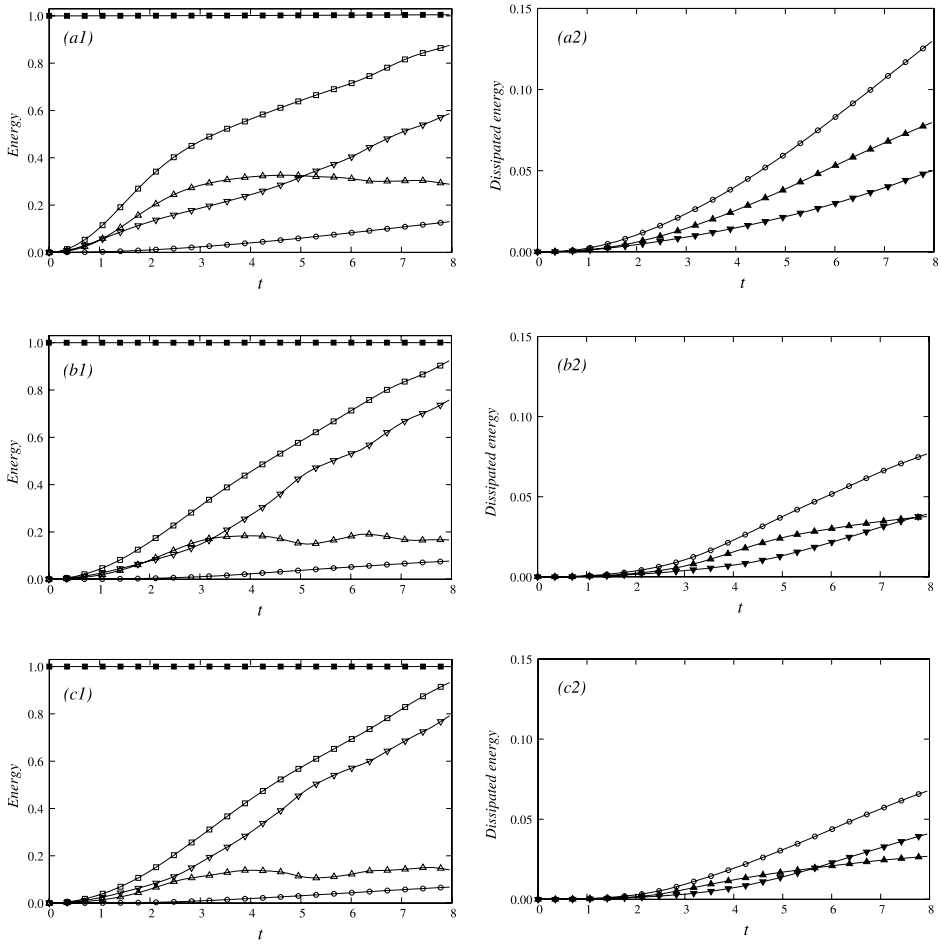

FIG. 9. The normalized total energy, kinetic energy, dissipated energy as functions of time for $\phi = 0.16$ and $Re = 4000$. Three different slope angles are chosen, i.e., $\theta = 9°, 40°,$ and $60°$, for illustrative purposes. All contributions to the energy budget are normalized by the potential energy loss from $t = 0$ to $t = 8$. The acceleration times for $\theta = 9°, 40°,$ and $60°$ are $t_c = 7.78, 6.01, 4.77$, respectively. Panels: top (a1 and a2), $\theta = 9°$; middle (b1 and b2), $\theta = 40°$; bottom (c1 and c2), $\theta = 60°$. Symbols: ■, total energy; □, kinetic energy K^n; △, kinetic energy associated with heavy fluid K_H^n; ▽, kinetic energy associated with ambient fluid K_L^n; ○, dissipated energy E_d^n; ▲, dissipated energy associated with heavy fluid E_{dH}^n; ▼, dissipated energy associated with ambient fluid E_{dL}^n.

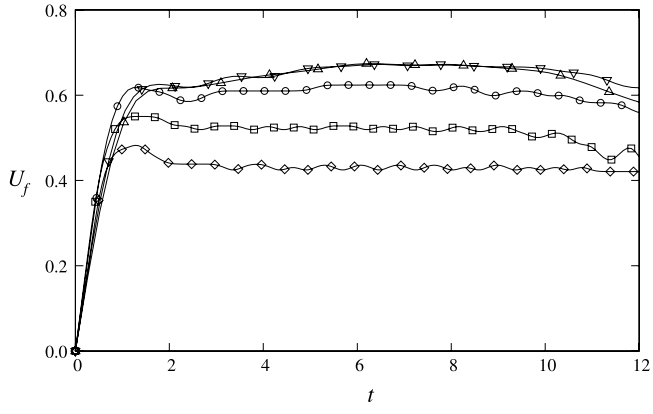

FIG. 10. Front velocity versus time for gravity currents propagating on a 9° slope at $Re = 4000$. Five different depth ratios are chosen for illustrative purposes. Symbols: △, $\phi = 0.075$; ▽, $\phi = 0.16$; ○, $\phi = 0.4$; □, $\phi = 0.7$; ◇, $\phi = 1$.

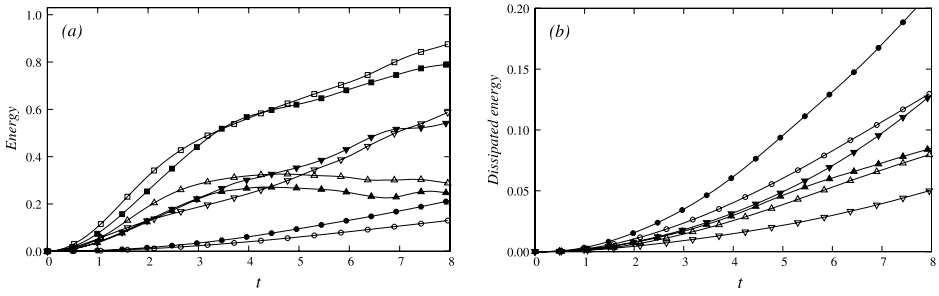

FIG. 11. The normalized kinetic energy and dissipated energy as functions of time for the case with $\theta = 9°$ and $Re = 4000$. Two different depth ratios, i.e., $\phi = 0.16, 1$, are chosen for illustrative purposes, where open symbols represent results from $\phi = 0.16$ and closed symbols represent those from $\phi = 1$. Panel (a) shows K^n, K^n_{dH}, K^n_{dL}, and E^n_d and panel (b) shows E^n_d, E^n_{dH}, and E^n_{dL}. Symbols in (a): □ and ■, kinetic energy K^n; △ and ▲, kinetic energy associated with heavy fluid K^n_H; ▽ and ▼, kinetic energy associated with ambient fluid K^n_L; ○ and ●, dissipated energy E^n_d. Symbols in (b): ○ and ●, dissipated energy E^n_d; ▲, dissipated energy associated with heavy fluid E^n_{dH}; ▼, dissipated energy associated with ambient fluid E^n_{dL}.

Figure 10 shows the front velocity versus time for five different depth ratios, i.e., $\phi = 0.075, 0.16, 0.4, 0.7$, and 1, while other parameters in the investigation remain unchanged as $\theta = 9°$ and $Re = 4000$. The flow domain is set as $L_{x_1} \times L_{x_3} = 10 l_0 \times \phi^{-1}$ and the grids used for $\phi = 0.075, 0.4, 0.7$, and 1 are listed in Table I. It is observed that, for $\phi = 1$, namely, the full-depth release, and for $\phi = 0.7$, the front velocity increases initially and falls slightly at $t \approx 1.4$ before approaching a quasi-steady phase, characterized by a constant front velocity, and followed by a deceleration phase. This quasi-steady phase persists for $t \gtrsim 2$ when $\phi = 1$ and for $2 \lesssim t \lesssim 9$ when $\phi = 0.7$. Here, the existence of a quasi-steady phase for a sufficiently large depth ratio, i.e., $\phi \geq 0.7$, is confirmed by the quasi-steady phase in the full-depth lock-exchange flow on a slope reported in Ref. 16. It is further observed here that the quasi-steady front velocity increases approximately from 0.43 to 0.52 as the depth ratio decreases from 1 to 0.7. As the depth ratio further decreases, i.e., $\phi \leq 0.4$, the gravity currents do not maintain a quasi-steady phase but continue to accelerate following the initial collapse of heavy fluid until reaching a maximum front velocity. It is worth noting the close agreement between the front velocity histories of $\phi = 0.16$ and $\phi = 0.075$, which indicates that $\phi = 0.16$ is a sufficiently good representation of the case of gravity currents in deep ambient, and also validates the experimental set-up in Ref. 19.

Figure 11 shows the comparison of the energy budgets for $\phi = 0.16$ and $\phi = 1$, where open symbols represent the results from $\phi = 0.16$ and closed symbols represent those from $\phi = 1$. For illustrative purposes, the energy budgets are plotted for and normalized with the potential energy drop during the initial eight dimensionless time units. As presented in Sec. III D, for $\phi < 1$, K^n_H grows faster than K^n_L initially before K^n_L overtakes K^n_H towards the end of the acceleration phase and the heavy fluid dissipates more energy than the ambient fluid in the acceleration phase. As the depth ratio increases, it is observed that more fraction of potential energy loss is converted into the kinetic energy associated with ambient fluid, less fraction of potential energy loss is converted into the kinetic energy associated with heavy fluid, and dissipated energy increases in both fluids. In fact, for the full-depth release, i.e., $\phi = 1$, the kinetic energy and dissipated energy are both equally distributed between the heavy and ambient fluids during the initial acceleration and early stage of the quasi-steady phase and the ambient fluid dissipates more energy than the heavy fluid in the later stage of the quasi-steady phase. From the energy analysis, it is observed that the conversion of potential energy loss into the kinetic energy associated with heavy fluid is inhibited and the conversion into the kinetic energy associated with ambient fluid and into dissipation appears to be enhanced by the confinement of the top wall.

F. Influence of the Reynolds number

In order to investigate the dependence of the flow on Re, we restrict our attention to the gravity currents on a 9° slope with $\phi = 0.16$. Figure 12 shows the density contours at $t = 4.42$ for the four Re-values of 100, 1000, 4000, and 10 000. The computational grids are listed in Table I. It is observed

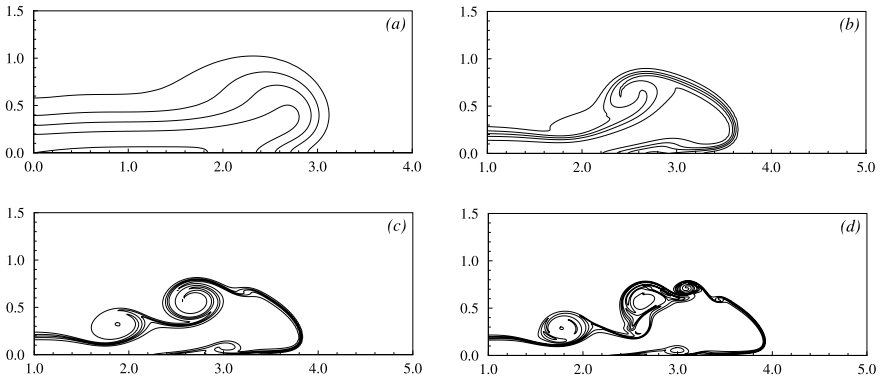

FIG. 12. Density contours at $t = 4.42$ for gravity currents propagating on a 9° slope with $\phi = 0.16$ at (a) $Re = 100$, (b) $Re = 1000$, (c) $Re = 4000$, and (d) $Re = 10\,000$.

that, as Re increases, the number of vortical structures over the boundary of the gravity current head increases. Furthermore, the two major roll-up vortices manifest themselves approximately at and above $Re \approx 4000$. Figure 13 shows the maximum front velocity versus Reynolds number for gravity currents on a 9° slope with $\phi = 0.16$. The maximum front velocity increases as Re increases and the influence of Re gradually diminishes as Re increases. In fact, the maximum front velocity increases by less than 5% as Re increases from 4000 to 10 000. One additional three-dimensional simulation of the gravity current on a 9° slope at $Re = 4000$ also confirms that two-dimensional runs faithfully represent the gravity current in the acceleration phase.

G. Buoyancy within the head

Buoyancy within the head has been observed to increase initially by addition of heavy fluid from the following current and to reach its maximum at the end of the acceleration phase. Previous experimental efforts to quantify the buoyancy within the head include Refs. 26 and 47. Much to our surprise, Ref. 47 reported that on a 10.6° slope, the maximum buoyancy within the head was approximately 44% of the buoyancy from a lock of $\tilde{l}_0/\tilde{h}_0 = 10$ cm/10 cm and approximately 35% of the buoyancy from a lock of 5.5 cm/9.7 cm. In contrast, Ref. 26 reported that the maximum buoyancy within the head was approximately between 75% and 82% for gravity currents on 6° and 9° slopes from a lock of 10 cm/8 cm. In this section, our computational data are used to clarify the controversy.

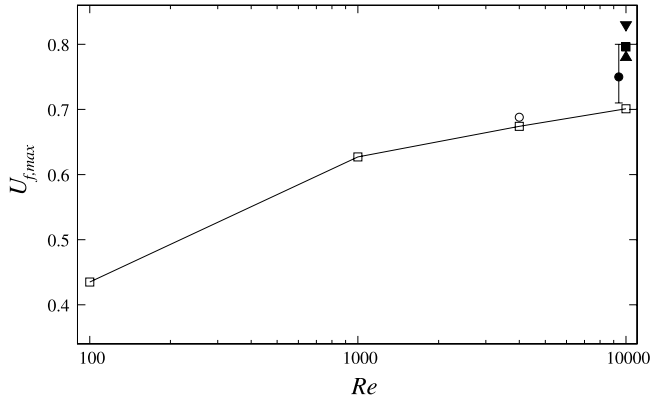

FIG. 13. Maximum front velocity versus Reynolds number for gravity currents propagating on a $\theta = 9°$ slope with $l_0 = 1.25$ and $\phi = 0.16$. Symbols: □, two-dimensional computational data; ○, three-dimensional computational data at $Re = 4000$; ■ experimental data from Ref. 19 for $l_0 = 1.25$ at $Re \approx 10^4$; ● experimental data from Ref. 26 for $l_0 = 1.25$ at $Re \approx 9400$; ▼, experimental data from Ref. 47 for $\theta = 10.6°$ and $l_0 \approx 2$ at $Re \approx 10^4$; ▲, experimental data from Ref. 47 for $\theta = 10.6°$ and $l_0 \approx 1$ at $Re \approx 10^4$.

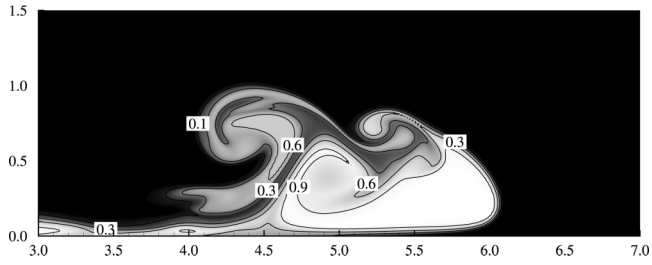

FIG. 14. Density distribution in the head of the gravity current propagating on a 9° slope at $t_c = 7.78$, when the maximum front velocity is reached, with $\phi = 0.16$ and $Re = 4000$. Solid lines represent the contours of $\rho = 0.1, 0.3, 0.6$, and 0.9 as inset numbers show.

Figure 14 shows the density distribution with contours for the gravity current head on a 9° slope at the end of the acceleration phase, i.e., $t_c = 7.78$. The roller is clearly seen in the region enclosed by the contour $\rho = 0.6$, which follows the less diluted head enclosed by the contour $\rho = 0.9$. It might appear difficult to draw the boundary between the gravity current head and ambient fluid due to the bulgy nature of the contours. To help visualize the distribution of buoyancy within the head, we use the threshold value of density contour, ρ_c, to define the boundary of the head. Therefore, the buoyancy within the head can be quantified as

$$B_H = \int_{x_f - L}^{x_f} \int_0^{L_{x_3}} \rho(x_1, x_3, t_c)|_{\rho \geq \rho_c} dx_3 dx_1, \tag{21}$$

where the integration is performed between the front location and the end of the head and within the head boundary defined by $\rho(x_1, x_3, t_c) \geq \rho_c$. The length of the head, L, in (21) is a variable distance between the front location and the end of the head, where the end of the head has to be determined by a subjective judgement, as done in previous studies. Note that the total dimensionless buoyancy is $B_0 = l_0$.

Figure 15 shows the ratio of buoyancy within the head, as shown in Figure 14, to the total buoyancy, B_H/B_0, versus the threshold value ρ_c. Due to mixing with ambient fluid as the gravity current propagates, the amount of heavy fluid in the head, of which the density exceeds 0.9 and which occupies the core region of gravity current head, is approximately only 30% of the total buoyancy. When the threshold value is lowered, the portion of heavy fluid within the head, of which the density exceeds ρ_c, increases to approximately 50% at $\rho_c = 0.6$ and to 70% at $\rho_c = 0.3$. The amount of mixed fluid, of which the density falls below $\rho_c = 0.2$, makes little contribution to the buoyancy within the head. As an example, in Figure 15, B_H/B_0 approaches 0.77 as $\rho_c \to 0$. Our computational analysis shows very good agreement with the experimental results by Ref. 26. It is very likely that in Ref. 47, only

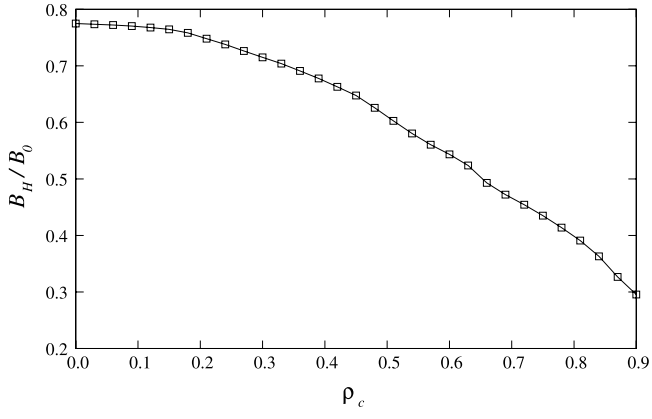

FIG. 15. Ratio of buoyancy within the head, as shown in Figure 14, to the total buoyancy, B_H/B_0, versus the threshold value, ρ_c, which defines the head boundary.

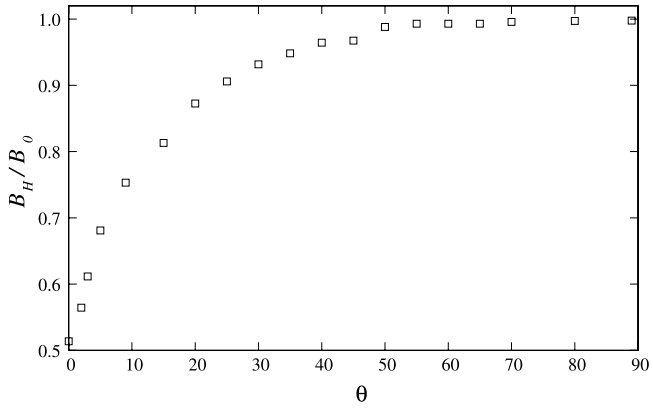

FIG. 16. Ratio of maximum buoyancy within the head to the total buoyancy, B_H/B_0, versus the slope angle, in units of degree. Gravity currents are produced from a lock of $l_0 = 1.25$ with $\phi = 0.16$ and $Re = 4000$. The threshold value chosen for the integration in (21) is $\rho_c = 0.01$.

the core region, e.g., that encircled by $\rho_c = 0.6$ in Figure 14, was taken as the gravity current head and the buoyancy within the head reported therein could be underestimated.

Figure 16 shows the dependence of B_H/B_0 on the slope angle. It is observed that B_H/B_0 increases monotonically with increasing slope angle. As the slope angle increases beyond approximately 25°, over 90% of the buoyancy in the lock is contained within the gravity current head at the end of the acceleration phase.

IV. CONCLUSIONS

The paper presents high-resolution two-dimensional Navier-Stokes simulations of gravity currents from instantaneous buoyancy sources propagating on different slope angles in the acceleration phase. Typically, in the laboratory the range of slope angle is limited by the flume height. In the simulations, investigations of gravity currents propagating on a slope in the entire range of $0° \le \theta < 90°$ become feasible.

Our results show that based on the front velocity history, after the heavy fluid is released from rest, the flow goes through the acceleration phase, reaching a maximum front velocity $U_{f,max}$, then followed by the deceleration phase. It is shown that the time of acceleration decreases with increasing slope angle, when the slope angle is approximately greater than 10° and for gravity currents on lower slope angles, the time of acceleration increases with increasing slope angle. The distinct characteristics are appropriately addressed by different scaling arguments, which is also supported by the fundamental difference in flow patterns between gravity currents on high and low slope angles.

Considering the substantial scatter in previously reported experimental data and the limited range of slope angle, previously the existence of a maximum of $U_{f,max}$ was not ascertained. The existence of a maximum of $U_{f,max}$ near $\theta = 40°$ is identified here unequivocally. Our observation is further reinforced by the novelly derived formula for $U_{f,max}$ that a maximum of $U_{f,max}$ could exist when the slope angle falls between 40° and 60°. With the help of energy analysis, it is shown that as the slope angle increases, the potential energy loss is more efficiently converted into the kinetic energy associated with ambient fluid, with less fraction of energy being converted into the kinetic energy associated with heavy fluid and being dissipated. Typically for gravity currents on lower slope angles, the heavy fluid contains more kinetic energy than the ambient fluid. As the slope angle increases beyond approximately 40°, the ambient fluid retains more kinetic energy than the heavy fluid, which also suggests the existence of a maximum $U_{f,max}$.

Here, a physical argument may help offer an insight into the role played by the slope angle. For gravity currents on a slope, while the streamwise component of gravity acts as the driving force, the wall-normal component of gravity stabilizes the flowing heavy fluid against unstable interface roll-up and vortex overturns with light ambient fluid. As the slope angle increases, not only the driving force

increases but also the stabilization provided by the wall-normal component of gravity diminishes. Both effects act to destabilize the interface between the heavy and light ambient fluids and explain that the mechanisms engaging ambient fluid, including interface roll-up and vortex overturns, are enhanced as the slope angle increases.

In the literature, gravity currents on a slope have been studied either in deep ambient or within a confined channel from a full-depth release. It is found that the latter part of the acceleration phase, which leads to a maximum front velocity, can be essentially annihilated, for sufficiently large depth ratios, and under such circumstances, the flow goes through a quasi-steady phase with a constant front velocity rather than reaching a maximum front velocity.

As the depth ratio increases, the conversion of potential energy loss into the kinetic energy associated with heavy fluid is inhibited and the conversion into the kinetic energy associated with ambient fluid and into dissipation is enhanced by the top wall confinement. In fact, for the full-depth releases, i.e., $\phi = 1$, the kinetic energy and dissipated energy are both equally distributed between the heavy and light ambient fluids during the initial acceleration and early stage of the quasi-steady phase.

In the present study, extensive investigations on gravity currents in the acceleration phase in the entire range of slope angles are possible thanks to the high-resolution two-dimensional Navier-Stokes simulations. It is understood that two-dimensional simulations are sufficiently representative for gravity currents in the acceleration phase, during which time three-dimensional interactions have been shown previously not important. Although the simulation results in the study show qualitative agreement with available experimental data, it should be noted that a discrepancy between the experimental data and the simulation results still exists and remains to be explained. For the propagation of gravity currents on a slope in the deceleration phase, the possibility of spanwise variations is likely to affect the flow and, as indicated by other computational studies,[18,22] three-dimensional simulations are required in that case. Efforts in this direction will be made when sufficient computational resources are available.

ACKNOWLEDGMENTS

The author wishes to thank the encouragement from Professor Paul Linden and Professor Stuart Dalziel at the University of Cambridge, S. Balachandar at the University of Florida, Marcelo Garcia and Gary Parker at the University of Illinois at Urbana-Champaign, C. C. Hsu at Tamkang University, and Bill Peirson at the University of New South Wales. The author also thanks Mr. Y. L. Huang for the help in preparing the figures. Computational resources are provided by National Taiwan University and Tamkang University. The research is funded in part by the Taiwan Ministry of Science and Technology through Grant No. NSC-101-2628-E-002-039-MY3 and by TSUNG Cho-chang Education Foundation through Grant No. 104-S-A10.

[1] J. Shin, S. Dalziel, and P. Linden, "Gravity currents produced by lock exchange," J. Fluid Mech. **521**, 1–34 (2004).
[2] B. Marino, L. Thomas, and P. Linden, "The front condition for gravity currents," J. Fluid Mech. **536**, 49–78 (2005).
[3] M. La Rocca, C. Adduce, G. Sciortino, and A. B. Pinzon, "Experimental and numerical simulation of three-dimensional gravity currents on smooth and rough bottom," Phys. Fluids **20**, 106603 (2008).
[4] M. La Rocca, C. Adduce, V. Lombardi, G. Sciortino, and R. Hinkermann, "Development of a lattice Boltzmann method for two-layered shallow-water flow," Int. J. Numer. Methods Fluids **70**, 1048–1072 (2012).
[5] M. La Rocca, C. Adduce, G. Sciortino, P. A. Bateman, and M. A. Boniforti, "A two-layer shallow water model for 3D gravity currents," J. Hydraul. Res. **50**, 208–217 (2012).
[6] C. Adduce, G. Sciortino, and S. Proietti, "Gravity currents produced by lock-exchanges: Experiments and simulations with a two layer shallow-water model with entrainment," J. Hydraul. Eng. **138**, 111–121 (2012).
[7] H. I. S. Nogueira, C. Adduce, E. Alves, and M. J. Franca, "Analysis of lock-exchange gravity currents over smooth and rough beds," J. Hydraul. Res. **51**, 417–431 (2013).
[8] H. I. S. Nogueira, C. Adduce, E. Alves, and M. J. Franca, "Image analysis technique applied to lock-exchange gravity currents," Meas. Sci. Technol. **24**, 047001 (2013).
[9] H. I. S. Nogueira, C. Adduce, E. Alves, and M. J. Franca, "Dynamics of the head of gravity currents," Environ. Fluid Mech. **14**, 519–540 (2014).
[10] J. Allen, *Principles of Physical Sedimentology* (Allen & Unwin, 1985).
[11] T. K. Fannelop, *Fluid Mechanics for Industrial Safety and Environmental Protection* (Elsevier, 1994).
[12] J. Simpson, *Gravity Currents*, 2nd ed. (Cambridge University Press, 1997).
[13] C. S. Jones, C. Cenedese, E. P. Chassignet, P. F. Linden, and B. R. Sutherland, "Gravity current propagation up a valley," J. Fluid Mech. **762**, 417–434 (2014).
[14] L. J. Marleau, M. R. Flynn, and B. R. Sutherland, "Gravity currents propagating up a slope," Phys. Fluids **26**, 046605 (2014).

[15] V. Lombardi, C. Adduce, G. Sciortino, and M. La Rocca, "Gravity currents flowing upslope: Laboratory experiments and shallow-water simulations," Phys. Fluids **27**, 016602 (2015).
[16] V. K. Birman, B. A. Battandier, E. Meiburg, and P. F. Linden, "Lock-exchange flows in sloping channels," J. Fluid Mech. **577**, 53–77 (2007).
[17] T. Seon, J. Znaien, B. Perrin, E. J. Hinch, D. Salin, and J. P. Hulin, "Front dynamics and macroscopic diffusion in buoyant mixing in tilted tubes," Phys. Fluids **19**, 125105 (2007).
[18] Y. Hallez and J. Magnaudet, "Effects of channel geometry on buoyancy-driven mixing," Phys. Fluids **20**, 053306 (2008).
[19] P. Beghin, E. J. Hopfinger, and R. E. Britter, "Gravitational convection from instantaneous sources on inclined boundaries," J. Fluid Mech. **107**, 407–422 (1981).
[20] R. E. Britter and P. F. Linden, "The motion of the front of a gravity current travelling down an incline," J. Fluid Mech. **99**, 531–543 (1980).
[21] A. Dai, C. E. Ozdemir, M. I. Cantero, and S. Balachandar, "Gravity currents from instantaneous sources down a slope," J. Hydraul. Eng. **138**, 237–246 (2012).
[22] A. Dai, "Gravity currents propagating on sloping boundaries," J. Hydraul. Eng. **139**, 593–601 (2013).
[23] T. Maxworthy and R. I. Nokes, "Experiments on gravity currents propagating down slopes. Part 1. The release of a fixed volume of heavy fluid from an enclosed lock into an open channel," J. Fluid Mech. **584**, 433–453 (2007).
[24] T. Bonometti, M. Ungarish, and S. Balachandar, "A numerical investigation of high-Reynolds number constant-volume non-Boussinesq density currents in deep ambient," J. Fluid Mech. **673**, 574–602 (2011).
[25] A. Dai and M. Garcia, "Gravity currents down a slope in deceleration phase," Dyn. Atmos. Oceans **49**, 75–82 (2010).
[26] A. Dai, "Experiments on gravity currents propagating on different bottom slopes," J. Fluid Mech. **731**, 117–141 (2013).
[27] A. Dai, "Non-Boussinesq gravity currents propagating on different bottom slopes," J. Fluid Mech. **741**, 658–680 (2014).
[28] M. R. Jacobson and F. Y. Testik, "On the concentration structure of high-concentration constant-volume fluid mud gravity currents," Phys. Fluids **25**, 016602 (2013).
[29] B. R. Morton, G. I. Taylor, and J. S. Turner, "Turbulent gravitational convection from maintained and instantaneous sources," Proc. R. Soc. A **234**, 1–23 (1956).
[30] W. B. Dade, J. R. Lister, and H. E. Huppert, "Fine-sediment deposition from gravity surges on uniform slopes," SEPM J. Sediment. Res. **64A**, 423–432 (1994).
[31] M. Rastello and E. J. Hopfinger, "Sediment-entraining suspension clouds: A model of powder-snow avalanches," J. Fluid Mech. **509**, 181–206 (2004).
[32] G. K. Batchelor, *An Introduction to Fluid Dynamics* (Cambridge University Press, 1967).
[33] T. H. Ellison and J. S. Turner, "Turbulent entrainment in stratified flows," J. Fluid Mech. **6**, 423–448 (1959).
[34] D. Webber, S. Jones, and D. Martin, "A model of the motion of a heavy gas cloud released on a uniform slope," J. Hazard. Mater. **33**, 101–122 (1993).
[35] G. Tickle, "A model of the motion and dilution of a heavy gas cloud released on a uniform slope in calm conditions," J. Hazard. Mater. **49**, 29–47 (1996).
[36] A. N. Ross, P. F. Linden, and S. B. Dalziel, "A study of three-dimensional gravity currents on a uniform slope," J. Fluid Mech. **453**, 239–261 (2002).
[37] C. Härtel, E. Meiburg, and F. Necker, "Analysis and direct numerical simulation of the flow at a gravity-current head. Part 1. Flow topology and front speed for slip and no-slip boundaries," J. Fluid Mech. **418**, 189–212 (2000).
[38] F. Necker, C. Härtel, L. Kleiser, and E. Meiburg, "Mixing and dissipation in particle-driven gravity currents," J. Fluid Mech. **545**, 339–372 (2005).
[39] M. Cantero, J. Lee, S. Balachandar, and M. Garcia, "On the front velocity of gravity currents," J. Fluid Mech. **586**, 1–39 (2007).
[40] T. Bonometti and S. Balachandar, "Effect of Schmidt number on the structure and propagation of density currents," Theor. Comput. Fluid Dyn. **22**, 341–361 (2008).
[41] V. K. Birman, J. E. Martin, and E. Meiburg, "The non-Boussinesq lock-exchange problem. Part 2. High-resolution simulations," J. Fluid Mech. **537**, 125–144 (2005).
[42] J. H. Williamson, "Low-storage Runge-Kutta schemes," J. Comput. Phys. **35**, 48–56 (1980).
[43] D. Durran, *Numerical Methods for Wave Equations in Geophysical Fluid Dynamics* (Springer, 1999).
[44] M. Cantero, S. Balachandar, and M. Garcia, "High-resolution simulations of cylindrical density currents," J. Fluid Mech. **590**, 437–469 (2007).
[45] C. Härtel, L. K. M. Michaud, and C. Stein, "A direct numerical simulation approach to the study of intrusion fronts," J. Eng. Math. **32**, 103–120 (1997).
[46] M. Ungarish, C. A. Mériaux, and C. B. Kurz-Besson, "The propagation of gravity currents in a V-shaped triangular cross-section channel: Experiments and theory," J. Fluid Mech. **754**, 232–249 (2014).
[47] T. Maxworthy, "Experiments on gravity currents propagating down slopes. Part 2. The evolution of a fixed volume of fluid released from closed locks into a long, open channel," J. Fluid Mech. **647**, 27–51 (2010).
[48] C. Cenedese and C. Adduce, "Mixing in a density driven current flowing down a slope in a rotating fluid," J. Fluid Mech. **604**, 369–388 (2008).
[49] K. B. Winters, P. N. Lombard, J. J. Riley, and E. A. D'Asaro, "Available potential energy and mixing in density-stratified fluids," J. Fluid Mech. **418**, 115–128 (1995).